

SmoCap: Unified Scale–Pose Canonicalization with Proxy-Mapped Trust-Region QP

Shihao Li* Naohiko Sugita

The Research into Artifacts, Center for Engineering, The University of Tokyo

*Corresponding author: lshdlut@gmail.com

Abstract

Objective: Stage-wise workflows that separate model scaling and inverse kinematics can induce morphology–posture compensation, resulting in anatomically inconsistent yet numerically acceptable solutions, especially in weakly observed directions. We present SmoCap, a leakage-resistant canonicalization framework that estimates morphology and posture jointly in each local trust-region quadratic program (QP) within a sparse control subspace. **Methods:** SmoCap solves a constrained trust-region QP with analytical proxy-mapped pose and scale Jacobians. The low dimensional proxy map stabilizes weakly observed directions and drives coordinated structures. An optional pre-solve provides warm starts in difficult configurations. The framework is evaluated using cohort fluoroscopy knee motion, anthropometric ground truth, and extreme yoga sequences. **Results:** SmoCap achieved 2.9° knee flexion RMSE against fluoroscopy, and a pooled anthropometric endpoint error around 3%. In the leakage audit against segment wise scaling, SmoCap also reduced marker RMSE, FE error, and anthropometric endpoint error. Proxy coupling preserved expressive and coordinated spine motion with marginal fitting error increase (+0.14 mm, +0.6%) against baseline models in yoga ablation. Median marker RMSE was around 20 mm, and median runtime was 0.204–0.332 ms/frame, achieved with consistently 2–3 iterations. **Conclusion:** SmoCap provides an externally validated unified coupling-aware scale–pose framework, making externally consistent motion canonicalization practical at dataset scale.

Keywords: motion capture, model scaling, trust-region quadratic programming, scale–pose leakage, fluoroscopy validation, musculoskeletal modeling

1 Introduction

Large-scale motion analysis is becoming increasingly important with recent advances in large-scale data-driven modeling and representation learning [1–3]. However, although the availability of human motion capture datasets has increased substantially, processing remains the main bottleneck. Separating morphology (scale) from kinematics (pose) with sufficient precision is nontrivial. The same marker or keypoint tracking error can be explained by different mixtures of shape and posture change when the pose and scale are not estimated jointly. The resulting trajectories are then anatomically inconsistent: segment lengths drift, joint behavior varies across sequences for the same subject, and the canonical motion representation breaks down. Here, motion canonicalization means mapping motions from different subjects and sessions into a shared and consistent parameter representation. There have been efforts to transform heterogeneous motion capture datasets into unified parameterizations (e.g., SMPL-based archives such as AMASS) highlighting the value of motion canonicalization [1, 2]. However, the pipeline was designed for a specific skin-model family, which limited sustained output [2]. At the same time, biomechanics, human body reconstruction, and control-oriented agile humanoid downstream pipelines increasingly require larger numbers of canonicalized human motion with coherent morphology and kinematics in a unified framework [4–7]. This highlights the need for a reliable separation

of scale and pose at scale with high throughput and practical accessibility.

Optical marker-based model reconstruction is widely recognized as a constrained optimization problem [8–10]. In practical trials, however, the problem is often mixed-determinate—some degrees of freedom (DoFs) are weakly observed and under informed, meanwhile others are locally over-constrained by dense but inconsistent marker observation. Thus, the difficulties are twofold: under informed parts are not uniquely identifiable, whereas over-constrained parts require the solver to arbitrate among contradictory residuals. This mixed-determinate setting leads to two connected failure modes: ambiguous residual allocation between morphology and posture, and unstable control of weakly observed DoFs.

The first challenge comes from morphology–posture residual allocation under different Jacobian conditioning and weights. The cascade path of this phenomenon is clear—morphology parameters such as segment dimensions and joint centers enter the same forward kinematics map as pose, and both can explain the same optimization residual, as shown by scaling studies on downstream kinematics and robustness [11–13]. Consequently, when one of them is fixed as a stage-wise precondition, residual can be absorbed by the other decision variable along near-singular directions, yielding anatomically invalid residual allocation across sequences, which we refer to as scale–pose leakage. Two-level calibration methods tried to alleviate this effect by wrapping scaling solves around repeated

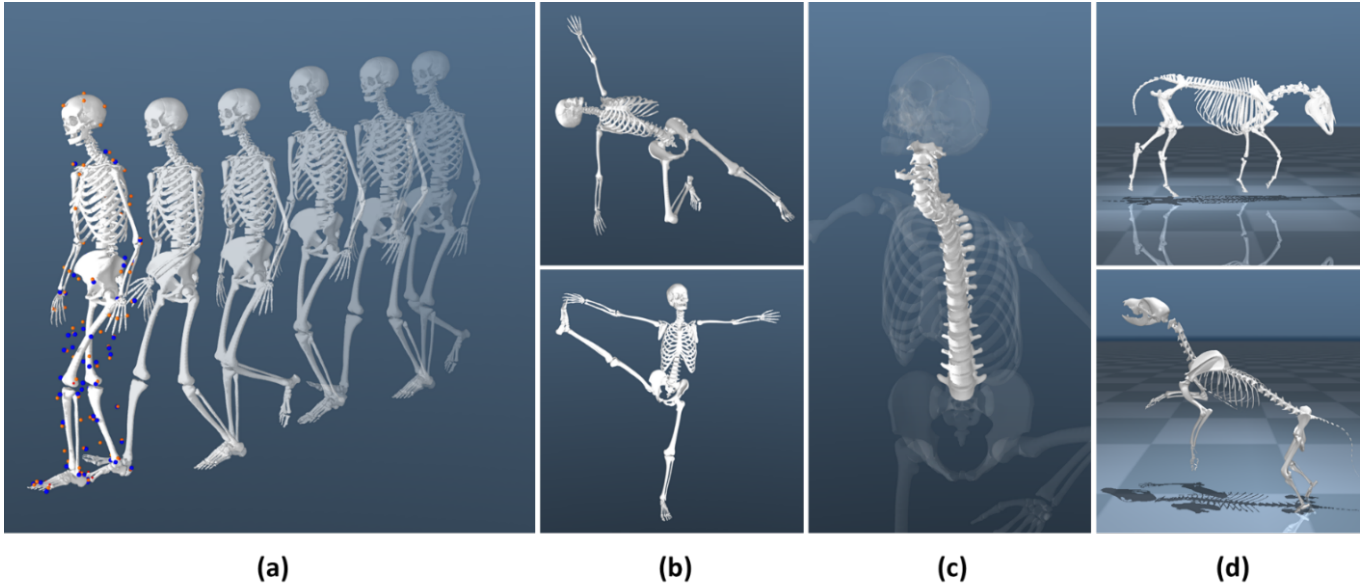


Figure 1: Representative outputs of SmoCap motion canonicalization. Motion and scale reconstruction: (a) human gait, (b) yoga poses, (c) proxy-mapped spine motion, and (d) quadruped motion examples. The quadruped examples use public dog motion capture and PFERD horse motion data [29, 30].

IK solves [14–16], while separated scale and pose parameter updates can still leave residual trade-offs. A simultaneous updating strategy was proposed by incorporating scale update with Schur complement into pose updates [17], yet the method requires a good initial guess to converge, and substantial variable space and runtimes are required (e.g., approximately 5 h for a 4680 frames trial with approximately 295,000 design variables). A unified scale–pose solver with good initialization and dataset scale throughput is still missing.

The second challenge is weak observability in coordinated

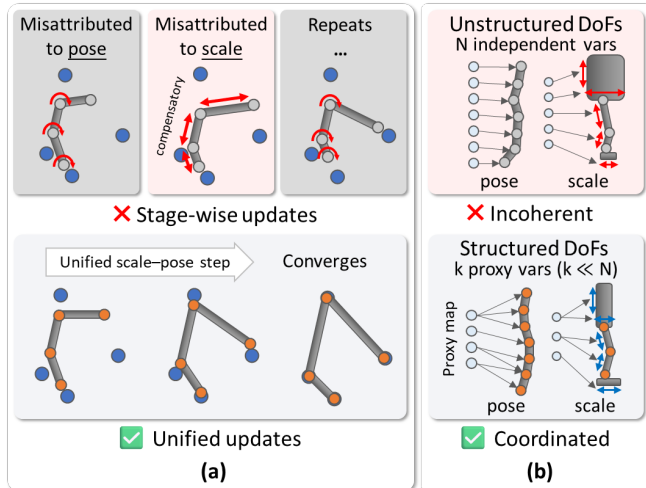


Figure 2: Design rationale under mixed determinacy. (a) Stage-wise updates can repeatedly assign residuals to pose or scale, whereas unified local scale–pose updates resolve both components simultaneously. (b) Under weak observability, independent high-DoF controls can produce incoherent internal motion, whereas proxy-coupled low dimensional controls coordinate structured DoFs.

anatomical structures of expressive models. This bottleneck is inherent to real-world scenarios, that structures often have far more properties than can be inferred from limited observation. An over parameterized model retaining many degrees of freedom has to rely on weight tuning and damping to resolve ambiguity; this preserves expressivity but can become brittle under marker noise, dropout, or small modeling changes, and can yield weight-driven artifacts and intermittent failures [9, 18]. Importantly, whether the system appears “over-determinate” globally or “under informed” locally, the practical symptom can be the same—near-singular or ill-conditioned Jacobians and pronounced sensitivity to weight choices [9]. This forces two opposing modeling responses. One is to reduce DoFs for identifiability at the cost of reduced expressivity, which becomes problematic for complex joints or diverse shapes [19–21]. The other is to retain many DoFs but leaves the coordinated structure implicit or even undealt. It often relies on weight or damping tuning, which becomes brittle and tuning dominated across noisy observations or small model changes.

Recent progress has led to more automated and versatile frameworks, yet coupling-aware capability under weak observability, and batch-scale reliability remain difficult. OpenCap similarly emphasizes a cloud processing workflow, but its kinematics are ultimately computed via inverse kinematics in OpenSim using a scaled musculoskeletal model [22]. AddBiomechanics formulates scaling and IK as a nonconvex bilevel MAP problem solved by IPOPT, requiring 3–5 minutes for pure morphological and kinematical solutions [23]. This becomes substantial at dataset scale, and the method further relies on a high quality initialization due to strong nonconvexity [23]. In parallel, differentiable biomechanics enables end-to-end fitting of scaling and IK within differentiable simu-

lators [24], and neural IK methods such as MANIKIN, which introduce strong priors via anatomically constrained, reduced-DoF representations on top of SMPL [1, 21]. These directions are highly valuable, but they shift the trade-off toward heavy additional optimization or training dependencies, that differ from an inspectable routine dataset scale canonicalization. Overall, recent advanced methods improved accessibility but still don't fully support (i) same-step scale-pose canonicalization, (ii) DoFs-coupling awareness under weak observability, and (iii) high-throughput and predictable batch processing ability.

The findings above point to a motion canonicalizer that can (i) provide leakage-resistant and externally auditable scale-pose canonicalization, (ii) flexibly encode naturally coordinated structures under mixed determinacy, and (iii) enable fast and predictable dataset scale throughput. We address this gap with SmoCap, a unified scale-pose canonicalizer built on explicit trust-region steps. Fig. 1 shows representative canonicalization outputs, and Fig. 2 shows the design rationale. In SmoCap, leakage resistance behavior is enabled by resolving morphology and posture under a unified local trust-region step, so that pose and scale will not be forced into sequential precedence; coordination is sustained by representing structured dependencies through a low dimensional subspace or soft referencing constraints. The solver runs at a sub-millisecond median per frame, and seconds-level for long trials. This fast, dataset scale throughput also benefits from the structured proxy mapping, which reduces effective problem dimension without sacrificing kinematic fidelity. Finally, for robustness in difficult trials, a light weight pre-solve solver that performs root-to-leaf sweeps of adjacent local subproblems in Gauss-Seidel style is used to yield a coherent warm start. Long range coupling and divergence are effectively reduced under mixed determinacy. In summary, we have four main contributions: a unified scale-pose TR-QP formulation, a proxy-mapped control subspace for coordinated DoFs, external pose-morphology validation with a leakage audit, and dataset scale throughput evaluation with optional pre-solve recovery.

2 Materials and methods

2.1 Notation

Symbol	Definition
$q \in \mathbb{R}^{n_q}$	Pose generalized coordinates
$s \in \mathbb{R}^{n_s}$	Morphology scale variables
$y = [q^\top, s^\top]^\top \in \mathbb{R}^{n_y}$	Full optimization variable
$x_{\text{obs}} \in \mathbb{R}^{n_x}$	Observed marker positions for the current frame
$\hat{x}(y) \in \mathbb{R}^{n_x}$	Model-predicted marker positions
$r_m(y) = \hat{x}(y) - x_{\text{obs}} \in \mathbb{R}^{n_x}$	Marker residual vector
$e_t(y) = y - y_{\text{ref}} \in \mathbb{R}^{n_y}$	Full-state tracking residual
$W_m \in \mathbb{R}^{n_x \times n_x}$	Square-root marker residual weight matrix
$W_t \in \mathbb{R}^{n_y \times n_y}$	Square-root full-space tracking weight matrix

$W_{\text{damp}} \in \mathbb{R}^{n_p \times n_p}$	Proxy-space damping weight matrix
$p \in \mathbb{R}^{n_p}$	Proxy variable in the reduced subspace
$\Phi(p) = y \in \mathbb{R}^{n_y}$	Mapping from proxy space to the full variable space
$J_y = \partial \hat{x} / \partial y \in \mathbb{R}^{n_x \times n_y}$	Marker Jacobian in the full variable space
$J_\Phi = \partial \Phi / \partial p \in \mathbb{R}^{n_y \times n_p}$	Jacobian of the proxy mapping
$J_m = J_y J_\Phi \in \mathbb{R}^{n_x \times n_p}$	Marker Jacobian in the proxy space
$\Delta p \in \mathbb{R}^{n_p}$	Bounded proxy-space step
ρ	Trust-region-style model agreement ratio

2.2 Solver overview

For each estimation problem, SmoCap requires 3D marker position observation x_{obs} , an articulated model that maps pose generalized coordinates q and body scale factor s , stacked as y , to model marker positions $\hat{x}(y)$. The unknown full state y is represented by low dimensional control variables p with a proxy mapping $y = \Phi(p)$. The residuals $r_m(y)$ are linearized at each iteration, forming a trust-region quadratic program (TR-QP) problem. TR-QP are box constrained when bounds are provided. The resulting step Δp is accepted when it gives a positive actual decrease, and the acceptance ratio ρ computed from actual and predicted decreases is used to update the trust-region damping. The estimation problem terminates when residual, relative decrease, or iteration reaches the threshold, and returns the estimated full state y as output.

Optionally, SmoCap includes (i) soft references tracking implemented as full-space tracking terms on y for tracking user specified priors, and (ii) a pre-solve that provides a warm start for TR-QP iterations in challenging configurations, such as entanglements caused by long-range coupling. The pre-solve is performed through root-to-leaf sweeps of overlapping local subproblems with Gauss-Seidel-style updates.

2.3 TR-QP problem formulation

SmoCap minimizes the marker objective, optionally with a tracking term, as below

$$E(y) = \frac{1}{2} \|W_m r_m(y)\|_2^2 + \frac{1}{2} \|W_t e_t(y)\|_2^2. \quad (1)$$

The problem is defined in the full state y , and optimized with proxy variable p through the mapping Φ , i.e., $\tilde{E}(p) := E(\Phi(p))$. The proxy map Φ specifies how reduced subspace variables control full pose-scale coordinates.

At each iterate, the marker residual is linearized as

$$r_m(y + \Delta y) \approx r_m(y) + J_y \Delta y, \quad \Delta y \approx J_\Phi \Delta p. \quad (2)$$

which yields the proxy-space approximation

$$r_m(\Phi(p + \Delta p)) \approx r_m(\Phi(p)) + J_m \Delta p. \quad (3)$$

where $J_m = J_y J_\Phi$. For $e_t(y) = y - y_{\text{ref}}$, the tracking increment is $J_\Phi \Delta p$.

SmoCap constructs the quadratic model in Δp as

$$m(\Delta p) = \frac{1}{2} \|W_m (J_m \Delta p + r_m)\|_2^2 + \frac{1}{2} \|W_t (J_\Phi \Delta p + e_t)\|_2^2 + \frac{1}{2} \|W_{\text{damp}}^{1/2} \Delta p\|_2^2. \quad (4)$$

where r_m , e_t , J_y , J_Φ , and J_m are evaluated at the current iterate, W_m and W_t are the marker and tracking square-root weight matrices, and W_{damp} applies per-coordinate regularization in the proxy space.

Expanding $m(\Delta p)$ gives the standard QP form

$$\min_{\Delta p} \frac{1}{2} \Delta p^\top H \Delta p + g^\top \Delta p. \quad (5)$$

where

$$H = J_m^\top W_m^\top W_m J_m + J_\Phi^\top W_t^\top W_t J_\Phi + W_{\text{damp}}, \quad (6)$$

$$g = J_m^\top W_m^\top W_m r_m + J_\Phi^\top W_t^\top W_t e_t.$$

The trust-region step solves a proxy-space QP with proxy-step bounds

$$\Delta p^* = \arg \min_{\Delta p} \frac{1}{2} \Delta p^\top H \Delta p + g^\top \Delta p, \quad (7)$$

subject to $\ell_b \leq \Delta p \leq u_b$.

Here ℓ_b and u_b are lower and upper proxy-step bounds. The predicted decrease is

$$\Delta f_{\text{pred}} = -g^\top \Delta p^* - \frac{1}{2} (\Delta p^*)^\top H \Delta p^*. \quad (8)$$

The actual decrease used for step acceptance is

$$\Delta f_{\text{act}} = \tilde{E}(p) - \left[\tilde{E}(p + \Delta p^*) + \frac{1}{2} \|W_{\text{damp}}^{1/2} \Delta p^*\|_2^2 \right]. \quad (9)$$

The acceptance ratio is computed as

$$\rho = \frac{\Delta f_{\text{act}}}{\Delta f_{\text{pred}} + \epsilon_\rho}. \quad (10)$$

where $\epsilon_\rho > 0$ is a small numerical stabilizer. If the actual decrease is non-positive, the trial step is rejected and shrunk; otherwise the step is accepted with $p \leftarrow p + \Delta p^*$, followed by $y \leftarrow \Phi(p)$. The ratio ρ is used to update the damping.

2.4 Implementation and complexity

Each iteration evaluates $\hat{x}(y)$ and residuals for m markers, computes Jacobians to form J_m , assembles (H, g) , solves a bounded proxy-space QP in n_p variables, and evaluates the step acceptance decrease. The dominant operations scale with marker count through forward kinematics and Jacobian evaluation, and with proxy dimension through the TR-QP size. The implementation uses MuJoCo for articulated model representation, kinematics, and box-constrained QP routines [25];

Algorithm 1. SmoCap per-frame solve

- 1: **Input:** marker observations, initial guess, proxy mapping, weights, bounds, termination thresholds
 - 2: **Output:** estimated full state and solver statistics
 - 3: Initialize the full state, proxy variables, and trust-region parameters.
 - 4: Optionally run the pre-solve to obtain a warm start.
 - 5: **repeat**
 - 6: Evaluate residuals and Jacobians.
 - 7: Assemble the proxy-space quadratic model.
 - 8: Solve the bounded proxy-space QP for the proxy step.
 - 9: Evaluate predicted and actual decreases, and the acceptance ratio.
 - 10: Accept/reject using the actual decrease; if accepted, update p and set $y = \Phi(p)$; update damping.
 - 11: **until** a termination criterion is met
 - 12: Return the final estimate and solver statistics.
-

additional implementation details are provided in the project repository, including JIT compilation, logging schema, engineering optimizations, and dataset-specific preprocessing.

2.5 Datasets and reference measurements

We use three datasets for evaluation. Dataset-specific preprocessing, synchronization, and alignment procedures are described in the project repository. The CAMS-Knee dataset provides synchronized optical marker trajectories together with fluoroscopy-derived femur and tibia motion measurements [26]; the Riglet dataset provides optical marker trajectories together with session anthropometric measurements [27]. The MoYo dataset provides yoga trials with extreme-pose marker trajectories [28].

2.6 Evaluation and reporting

The evaluation is threefold: external scale–pose consistency with leakage audit, coordinated structure under weak observability, and throughput. Trial-level results are presented with robust statistics (median and 95th percentile). For scale–pose consistency, we report marker fit together with external pose and morphology references [31]. Marker RMSE is reported under a dataset level shared marker-registration model without subject- or trial-specific marker-offset optimization [32, 33]. Pose is evaluated as Grood–Suntay knee kinematics derived from fluoroscopy [34], and morphology is evaluated against direct anthropometric endpoints. Leakage audit was performed by comparing SmoCap with an OpenSim style stage and segment wise scaling baseline [35, 36], using the same external pose and morphology references.

For coordinated structure preservation, we use MoYo dataset to perform a spine DoFs coupling ablation [19]. Three configurations were compared: proxy variables controlled DoFs full spine via polynomial mapping (poly), independent DoFs full spine (nopoly), and a reduced three-segment spine (classical). We report marker error, coordination plausibility statistics such as spatial and temporal roughness of spine DoFs, and lumbopelvic-rhythm measures.

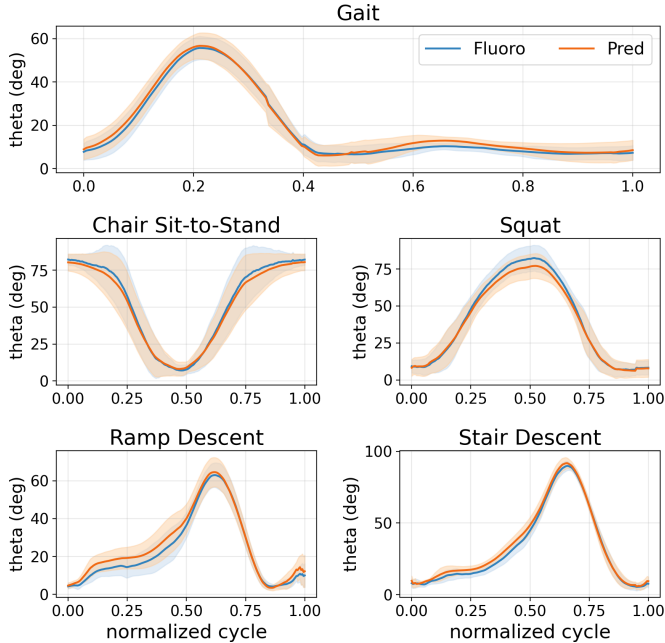


Figure 3: Fluoroscopy-based knee kinematics validation. SmoCap predicted knee flexion trajectories are compared with fluoroscopy-derived references across gait, chair sit-to-stand, squat, ramp descent, and stair descent. Trajectories are shown over normalized cycles, with shaded regions showing cross-trial variation.

For throughput and convergence statistics, we report per-frame and dataset level runtime, together with solver statistics.

3 Results

3.1 Results outline

We present results along three axes. First, we evaluate external pose–morphology consistency on CAMS-Knee and Riglet datasets, including a leakage audit against a segment wise scaling baseline. The evaluation is done using fluoroscopy knee kinematics, CT registered and hand measured anthropometric endpoints. Second, we report a kinematical spine ablation on MoYo dataset to evaluate proxy variable driven behavior under weak observability. Third, we report throughput and convergence statistics, and the optional pre-solve warm-start performance across CAMS-Knee, Riglet, and MoYo dataset.

3.2 Fluoroscopy and anthropometry-based external validation and leakage audit

Aggregated fluoroscopy kinematics reference and predictions of knee joint angle trajectory, as the pose estimation validation, are shown in Fig. 3. The predicted trajectories align closely with fluoroscopy reference in both phase and shape across the normalized multitask gait cycles. Despite the overall high agreement, mild shape deviations are observed around deep squat and lower-flexion regions of ramp descent. Apart from aggregation, per-trial errors remain an overall narrow range, with a typical error magnitude of approximately $3\text{--}4^\circ$.

Table 1: Contextual comparison with reported tibiofemoral flexion validation.

Research	Non-invasive	Deep flexion	FE error ($^\circ$)
SmoCap	Yes	Yes	2.9
Reinschmidt et al. [37]	No	No	2.1
Tranberg et al. [38]	No	No	2–5
Fändriks et al. [39]	No	Yes	5–15
Wang et al. [40]	Yes	No	1.4

Table 2: Leakage audit against an OpenSim style segment wise scaling baseline.

Mode	Marker		FE		Anthropometry	
	RMSE	Wins	RMSE	Wins	MAE	Wins
SmoCap	18.81 mm	28/28	2.87 $^\circ$	23/28	7.24 mm	23/28
OpenSim style	25.95 mm	0/28	3.87 $^\circ$	5/28	11.30 mm	5/28

Marker RMSE, fluoroscopy-based flexion-extension (FE) error, and anthropometric endpoint error are compared under the same setting. “Wins” denotes the number of trials with lower error.

As a contextual comparison with prior ground-truth studies, SmoCap yielded comparable results without invasive instrumentation, as shown in Table I. Typical workflows for obtaining skeletal ground truth rely on invasive measures such as bone pins or implanted tantalum markers [37–39]. In contrast, our evaluation is performed only with skin markers, while covering deep-flexion functional activities including squat and sit to stand. The reported FE error in our results (RMSE $\approx 2.9^\circ$) are on the same level as classical walking validations (e.g., approximately 2° mean difference in bone-pin studies), and are substantially lower than those reported in high flexion RSA validations ($5\text{--}15^\circ$ mean differences).

Anthropometric endpoints error distributions as an external validation on scale estimation, are shown in Fig. 4 for CAMS-Knee and Riglet datasets. Signed anthropometric errors for most metrics are centered near zero with no systematic bias across metrics. The median or absolute percentage errors were low overall: most around 0–3% level, while higher errors appeared at narrower or weakly observed metrics such as elbow width. Also, lower base length resulted in higher percentage error for width-like metrics. These endpoints provide an independent validation of scale estimation apart from the pose estimation validation and indicate that the estimated scale parameters remain compatible with the external measurements.

Scale–pose leakage was audited against an OpenSim style stage and segment wise scaling and IK baseline under the same condition [35, 36]. As shown in Table II, SmoCap achieved lower marker RMSE, fluoroscopy-based FE error, and anthropometric endpoint error against the OpenSim style baseline.

3.3 Proxy ablation under weak observability for naturally coordinated structures

We used MoYo dataset, which includes extreme and large amplitude poses but only with sparse surface markers [28], to evaluate the proxy variable driven behavior under weak observability. In particular, the multi-DoF yet naturally coordi-

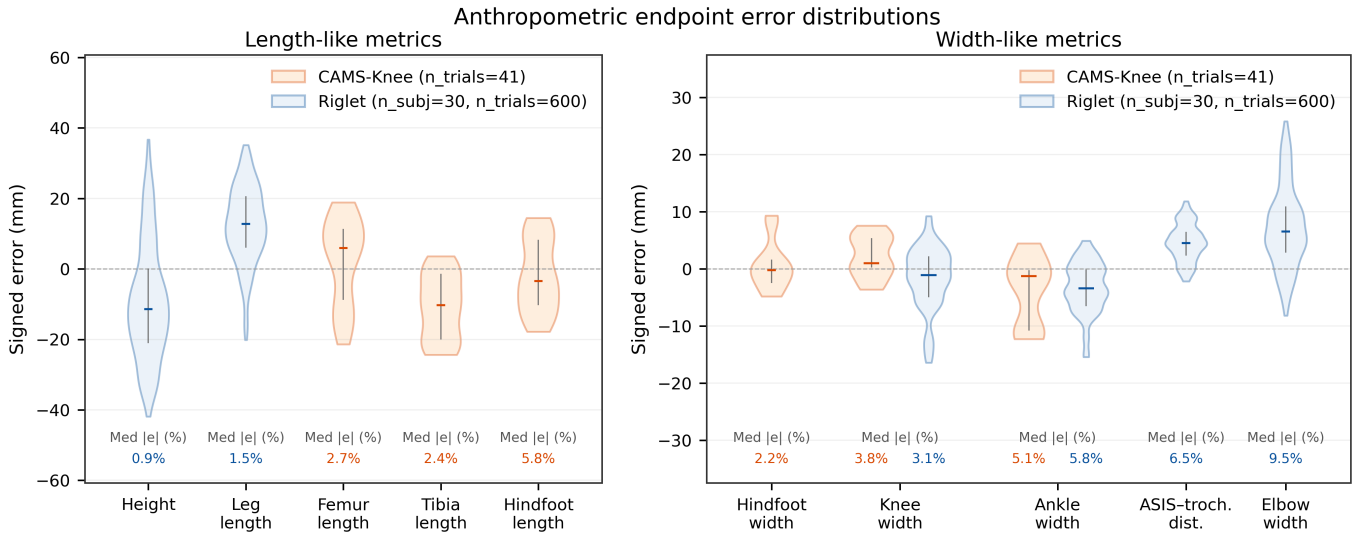


Figure 4: Anthropometric endpoint error distributions for external morphology validation. Signed endpoint errors are shown for length-like and width-like metrics on CAMS-Knee and Riglet datasets. Violin distributions summarize endpoint errors, and median absolute percentage errors are reported below.

nated spine structures can only be constrained indirectly, which creates a weakly observed setting. We compare three spine modes: poly, in which spine DoFs are coordinated through proxy mapping; nopoly, in which spine DoFs are independent; and classical, in which the spine is reduced to rigid segments. All configurations are evaluated on the same sequences. Because MoYo has no ground truth spine reference, roughness and bending-pattern measures are treated as solver-behavior proxies rather than biological ground truth. The ablation using plausibility proxies, tracking error, and runtime metrics are summarized in Fig. 5.

Fig. 5A shows the temporal roughness of per joint angle history, and spatial roughness of spine at each time instant. Poly exhibits lower roughness overall. In contrast, nopoly formed a separated high-roughness cluster, whereas classical was temporally smooth but spatially rougher.

Fig. 5B reports relative marker fitting error of poly and nopoly against classical. Poly is close to classical (median $\Delta\text{RMSE} = +0.14$ mm, $+0.6\%$), whereas nopoly shows a mild reduction in RMSE (median $\Delta\text{RMSE} = -0.73$ mm, -3.2%). Thus, significantly lower roughness can be achieved with configurations with similar marker errors.

Fig. 5C compares runtime across configurations. Median runtime was 0.35 ms/frame for poly (DoFs = 5), 0.30 ms/frame for classical (DoFs = 8), and 16.12 ms/frame for nopoly (DoFs = 72). Poly and classical remain at a similar level, while nopoly leads to substantially higher computational cost.

Fig. 6 shows distinct spine bending patterns: poly is smooth and globally distributed, nopoly shows fragmented and poorly coordinated local bending, and classical exhibits a piecewise and broken pattern with rigid segments.

Taken together, Figs. 5–6 show that under weak observability, proxy coupling leads to more naturally coordinated behavior without materially increasing fitting error and computational cost.

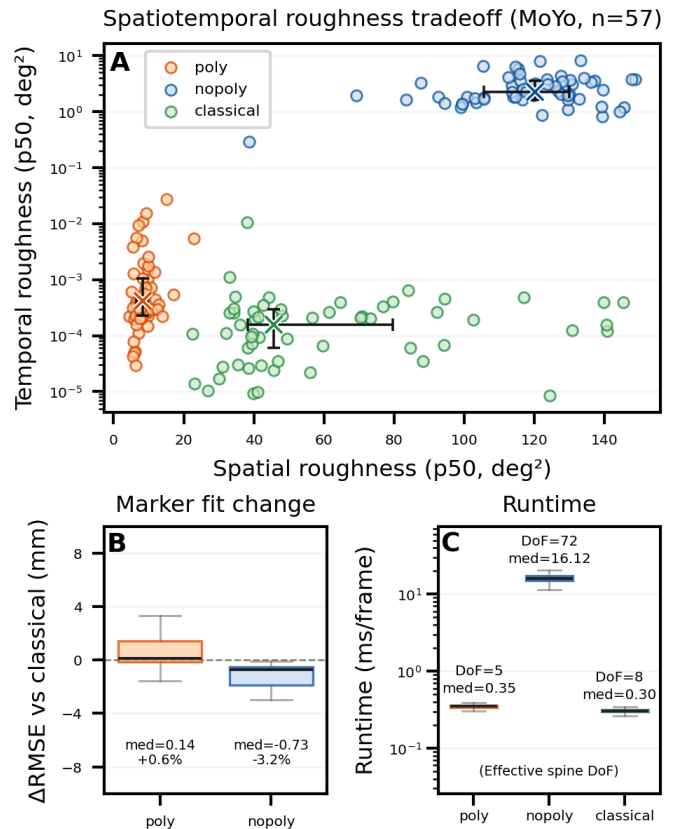


Figure 5: Proxy ablation under weak observability. (A) Spatiotemporal spine roughness for the proxy-coupled spine (poly), independent-DoF spine (nopoly), and segmented spine (classical). (B) Marker-fit change relative to the segmented-spine baseline. (C) Runtime across the three spine configurations.

3.4 Throughput and convergence across different motion

Table III summarizes throughput across CAMS-Knee, Riglet, and MoYo datasets. Sub-millisecond per-frame runtime

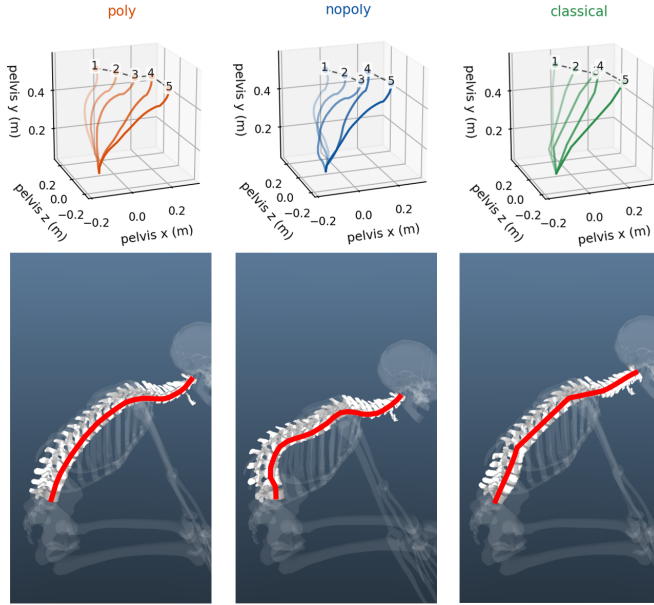


Figure 6: Spine bending patterns under different spine configurations. Top: spine curves at five sampled time points. Bottom: skeleton render at a representative frame. The proxy-coupled spine (poly) shows smooth distributed curvature, the independent-DoF spine (nopoly) shows fragmented local bending, and the segmented spine (classical) shows piecewise rigid bending.

Table 3: Default throughput and convergence statistics across datasets.

Dataset	Frames	FPS	Time (ms)		Iters		RMSE (mm)	
			p50	p90	p50	p90	p50	p90
CAMS-Knee	10740	4902	0.204	0.301	2	3	18.2	20.6
Riglet	10138	3353	0.298	0.383	3	3	17.8	21.1
MoYo	11698	3013	0.332	0.498	2	3	25.8	32.4

Per-frame solver runtime with file I/O and model loading excluded.

was achieved across all datasets (0.204, 0.298, and 0.332 ms, respectively), with highest p90 runtime 0.5 ms in MoYo. Average per frame iterations bounded at 2 to 3. Riglet reported lowest marker RMSE (17.8/21.1 mm, p50/p90), followed by CAMS-Knee. MoYo had the highest error, consistent with its challenging yoga poses. In conclusion, the overall convergence performance remained stable at a high level across distinct datasets.

3.5 Pre-solve warm-start performance across datasets

The ablation results for pre-solve, as a warm-start state, were shown in Table IV. For each dataset, outliers were defined as marker-RMSE values that exceed the no-pre median by 6 MADs, and the same threshold was applied to the pre-solve runs. Pre-solve increased cold start runtime by around 3–7 times for CAMS-Knee, Riglet, and MoYo dataset, but consistently reduced outlier rates. MoYo showed largest reduction, where outliers decreased from 18.33% to 5.93%. CAMS-Knee and Riglet were already low without pre-solve, and still de-

Table 4: Pre-solve warm-start performance.

Dataset	Frames	Overhead (\times)	Pre (ms)		Out. (%)		
			p50	p90	No-pre	Pre	Δ
CAMS-Knee	1500	3.28	5.010	6.221	4.53	1.87	2.67
Riglet	1500	4.54	9.127	10.288	0.13	0	0.13
MoYo	1500	7.39	12.677	14.527	18.33	5.93	12.40

creased to 1.87% and 0%, respectively. Overall, SmoCap performed stably in regular cases, while the optional pre-solve reduces failures in difficult configurations.

4 Discussion

We aim to address a key problem in large scale motion analysis with this work: a good marker fit does not necessarily lead to externally valid pose or morphology [31]. When scale and pose are treated separately, tracking residuals can be resolved with morphology–posture compensation along weakly observed directions, generating anatomically inconsistent yet numerically acceptable results. This downgrades the fidelity for cross trial kinematical and morphological comparability, and downstream motion imitation and biomechanics applications. To address this, we proposed a unified framework that resolves scale and pose jointly in the same trust-region step, while naturally coordinated or weakly observed DoFs are controlled through proxy coupling. For evaluation, we probed simulation-external reference consistency, weak observability behavior, and practical scalability. Pose and morphology consistency are confirmed with external fluoroscopy and anthropometric measurements (Results B). Proxy controlled DoFs can yield plausible solution under weak observability (Figs. 5–6). Dataset-scale usability was assessed through throughput, convergence statistics, and whether a light weight warm start pre-solve can reduce failures in difficult regimes (Table IV).

Fluoroscopy and anthropometric data are two kinds of independent external measurements of kinematics and scale [41,42]. Thus the pipeline’s output can be validated with those real measurements rather than only tested on internal consistency. In fluoroscopy validation, the calculated knee kinematics align closely with reference across tasks including deep flexion activities with errors around few degrees (Results B). At the same time, anthropometric endpoint errors are centered near zero and remain small in percentage. Taken together, the low marker error is observed together with independently valid pose and morphology estimates. Together with the leakage audit, this suggests that the fit is not achieved by arbitrary morphology–posture compensation. This is why we evaluate the recovered pose and scale components separately against independent external ground truth, rather than relying only on marker residuals.

The reported marker RMSE should be interpreted under our registration setting. We used a shared marker offset model in each dataset and did not perform subject-specific manual marker adjustment or marker-offset optimization [32,33]. Manual adjustment harms scalability to large datasets, while marker

offset optimization is highly under-constrained and can absorb residual without identifying sources. Even under our setting, SmoCap achieved good external agreement, which further demonstrated that the reconstruction quality is not judged by marker residual alone.

The spine ablation under extreme yoga poses provides the view of why proxy coupling, which represents naturally coordinated DoFs, is important. Spine is a natural high DoFs yet not fully independent structure [19]. Given the fact that spine DoFs can't be fully constrained with ordinary sparse marker set, researchers must face the tradeoff between less expressive model with segmented rigid spines, which we call classical, or less predictable and computationally heavy model with full DoFs, which we call nopoly. Thus, we compare the poly model, whose free DoFs are driven by proxy variables, yet can retain expressive curvatures, with the classical and nopoly models. Figs. 5–6 show that poly, nopoly, and classical can achieve similar marker fits while yielding distinct spine patterns in roughness, morphology, and computation. Compared with classical, poly marker RMSE only changes marginally by +0.14 mm (+0.6%), yet it achieves significantly lower roughness (Fig. 5A) at near-identical runtime (0.35 ms/frame vs 0.30 ms/frame). Nopoly achieves the lowest marker fit error but produces fragmented local bending patterns and incurs a two order higher runtime (16.12 ms/frame). The key point here is that lower marker RMSE alone does not necessarily indicate a better solution, and expressiveness cannot be achieved simply by adding DoFs, but should be together with controlling how weakly observed internal freedom is coordinated. Accordingly, proxy coupling should not be viewed only as a heuristic. It coordinates expressive DoFs in ambiguous subproblems and guides the solution toward a more natural basin, while keeping fitting error and runtime close to the more deterministic baseline.

Throughput performance is a key feature of SmoCap. It makes dataset scale canonicalization cheap enough to become routine. Prior works have also treated computational speed as a key problem [14, 15, 17, 43]; AddBiomechanics reports 3–5 min for scaling and kinematics alone, OpenCap reports 2 min for single-squat kinematics after data collection, and differentiable biomechanics optimization can take several minutes for typical sessions [22–24]. In contrast, SmoCap runs at sub-millisecond per frame with only 2–3 iterations, so a typical 10 s, 100 Hz trial can be canonicalized in roughly 0.3–0.5 s. Batch processing becomes so inexpensive, that it can be used as a standard preprocessing primitive for dataset scale pipelines rather than a fragile offline calibration step.

A remaining practical bottleneck is extreme configuration reconstruction. SmoCap is already robust in ordinary cases with near zero outlier as shown in Table IV, while situations like twisted configurations or weak initiation can still lead to obviously poor local minima. The pre-solve stage, as a warm start strategy, is designed for this issue. It is based on Gauss–Seidel style root-to-leaf local sweeps that can effectively untangle complex configurations, especially when constraints are present. The runtime just grows several-fold with an already very low base, making it applicable difficult configurations

or suspicious residuals are observed. Its value is clearest on MoYo, where many bad solutions can be rescued, as reflected by outlier reduction from 18.33% to 5.93%.

Several limitations should be stated here. First, this is a marker-based estimation pipeline, which relies on corresponding marker definitions between the model and the target, together with a rigid marker-offset assumption. This means that extreme marker displacement such as marker pair placement error or soft tissue artifact can reduce robustness [41, 44–46]. Second, we did not include inertia related or musculotendinous scale as this study focuses on morphology–motion canonicalization. This may affect the direct applicability for dynamic tasks, while body mass scaling or actuator parameter tuning (e.g. hill muscle) can be incorporated using existing scaling methods, but were outside of our scope [43, 47–51]. Third, the spine ablation evaluates plausibility through spatiotemporal roughness and morphology rather than imaging-based or statistical ground truth. Those metrics are informative for solver behavior, but they do not certify biological correctness clinically.

Future directions are indicated with the limitations stated above. The idealized marker placement and rigid marker transform assumption should be reduced or eliminated with richer anatomy-aware priors or models, such that scale and pose remain identifiable even when these idealized assumptions do not hold. The dynamics related attributes scaling should also be included under the same unified formulation. This would make the framework beyond morphology–motion canonicalization without breaking the kinematic dynamic consistency.

Overall, SmoCap provides a unified and scalable formulation for motion canonicalization that resolves morphology and motion within the same optimization framework. By controlling naturally coordinated DoFs through proxy coupling and warm starting through light weight pre-solve, SmoCap makes externally consistent large-scale motion reconstruction practical even under weakly observed ambiguous behavior and extreme configurations.

Data and Code Availability

The reference implementation, scripts for reproducing the reported figures and tables, and result artifacts are available at: <https://github.com/lshdlut/smocap-paper-artifact>. The Python implementation of the SmoCap solver is available at: <https://github.com/lshdlut/smocap-paper-code>. An interactive demonstration is available at: <https://lshdlut.com/SmoCap>. The original datasets are not redistributed; dataset access follows the licenses and access policies of the original data providers.

Competing interests

None.

References

- [1] M. Loper, N. Mahmood, J. Romero, G. Pons-Moll, and M. J. Black, “SMPL: A skinned multi-person linear model,” *ACM Trans. Graph.*, vol. 34, no. 6, pp. 1–16, 2015, doi: 10.1145/2816795.2818013.
- [2] N. Mahmood, N. Ghorbani, N. F. Troje, G. Pons-Moll, and M. J. Black, “AMASS: Archive of motion capture as surface shapes,” in *Proc. IEEE/CVF Int. Conf. Comput. Vis.*, 2019, pp. 5442–5451.
- [3] X. Han, B. Senderling, S. To, D. Kumar, E. Whiting, and J. Saito, “GroundLink: A dataset unifying human body movement and ground reaction dynamics,” in *Proc. SIGGRAPH Asia Conf. Papers*, 2023, pp. 1–10, doi: 10.1145/3610548.3618247.
- [4] W. R. Johnson, A. Mian, D. G. Lloyd, and J. A. Alderson, “On-field player workload exposure and knee injury risk monitoring via deep learning,” *J. Biomech.*, vol. 93, pp. 185–193, 2019, doi: 10.1016/j.jbiomech.2019.07.002.
- [5] X. B. Peng, P. Abbeel, S. Levine, and M. van de Panne, “DeepMimic: Example-guided deep reinforcement learning of physics-based character skills,” *ACM Trans. Graph.*, vol. 37, no. 4, pp. 1–14, 2018, doi: 10.1145/3197517.3201311.
- [6] Z. Luo, J. Cao, A. Winkler, K. Kitani, and W. Xu, “Perpetual humanoid control for real-time simulated avatars,” in *Proc. IEEE/CVF Int. Conf. Comput. Vis.*, 2023, pp. 10861–10870, doi: 10.1109/ICCV51070.2023.01000.
- [7] B. J. Fregly, J. A. Reinbolt, K. L. Rooney, K. H. Mitchell, and T. L. Chmielewski, “Design of patient-specific gait modifications for knee osteoarthritis rehabilitation,” *IEEE Trans. Biomed. Eng.*, vol. 54, no. 9, pp. 1687–1695, 2007, doi: 10.1109/TBME.2007.891934.
- [8] T. W. Lu and J. J. O’Connor, “Bone position estimation from skin marker co-ordinates using global optimisation with joint constraints,” *J. Biomech.*, vol. 32, no. 2, pp. 129–134, 1999, doi: 10.1016/S0021-9290(98)00158-4.
- [9] M. S. Andersen, M. Damsgaard, and J. Rasmussen, “Kinematic analysis of over-determinate biomechanical systems,” *Comput. Methods Biomech. Biomed. Eng.*, vol. 12, no. 4, pp. 371–384, 2009, doi: 10.1080/10255840802459412.
- [10] S. Duprey, L. Chèze, and R. Dumas, “Influence of joint constraints on lower limb kinematics estimation from skin markers using global optimization,” *J. Biomech.*, vol. 43, no. 14, pp. 2858–2862, 2010, doi: 10.1016/j.jbiomech.2010.06.010.
- [11] M. E. Lund, M. S. Andersen, M. de Zee, and J. Rasmussen, “Scaling of musculoskeletal models from static and dynamic trials,” *Int. Biomech.*, vol. 2, no. 1, pp. 1–11, 2015, doi: 10.1080/23335432.2014.993706.
- [12] D. Bakke and T. Besier, “Shape model constrained scaling improves repeatability of gait data,” *J. Biomech.*, vol. 107, 2020, Art. no. 109838, doi: 10.1016/j.jbiomech.2020.109838.
- [13] D. Bakke, P. Ortega-Auriol, and T. Besier, “Shape-model scaling is more robust than linear scaling to marker placement error,” *J. Biomech.*, vol. 160, 2023, Art. no. 111805, doi: 10.1016/j.jbiomech.2023.111805.
- [14] I. W. Charlton, P. Tate, P. Smyth, and L. Roren, “Repeatability of an optimised lower body model,” *Gait Posture*, vol. 20, no. 2, pp. 213–221, 2004, doi: 10.1016/j.gaitpost.2003.09.004.
- [15] J. A. Reinbolt *et al.*, “Determination of patient-specific multi-joint kinematic models through two-level optimization,” *J. Biomech.*, vol. 38, no. 3, pp. 621–626, 2005, doi: 10.1016/j.jbiomech.2004.03.031.
- [16] J. A. Reinbolt, R. T. Haftka, T. L. Chmielewski, and B. J. Fregly, “A computational framework to predict post-treatment outcome for gait-related disorders,” *Med. Eng. Phys.*, vol. 30, no. 4, pp. 434–443, 2008, doi: 10.1016/j.medengphy.2007.05.005.
- [17] M. S. Andersen, M. Damsgaard, B. MacWilliams, and J. Rasmussen, “A computationally efficient optimisation-based method for parameter identification of kinematically determinate and over-determinate biomechanical systems,” *Comput. Methods Biomech. Biomed. Eng.*, vol. 13, no. 2, pp. 171–183, 2010, doi: 10.1080/10255840903067080.
- [18] M. Damsgaard, J. Rasmussen, S. T. Christensen, E. Surma, and M. de Zee, “Analysis of musculoskeletal systems in the AnyBody Modeling System,” *Simul. Model. Pract. Theory*, vol. 14, no. 8, pp. 1100–1111, 2006, doi: 10.1016/j.simpat.2006.09.001.
- [19] M. de Zee, L. Hansen, C. Wong, J. Rasmussen, and E. B. Simonsen, “A generic detailed rigid-body lumbar spine model,” *J. Biomech.*, vol. 40, no. 6, pp. 1219–1227, 2007, doi: 10.1016/j.jbiomech.2006.05.030.
- [20] J. Li, C. Xu, Z. Chen, S. Bian, L. Yang, and C. Lu, “HybrIK: A hybrid analytical-neural inverse kinematics solution for 3D human pose and shape estimation,” in *Proc. IEEE/CVF Conf. Comput. Vis. Pattern Recognit.*, 2021, pp. 3383–3393.
- [21] J. Jiang, P. Strela, X. Luo, C. Gebhardt, and C. Holz, “MANIKIN: Biomechanically accurate neural inverse kinematics for human motion estimation,” in *Computer Vision – ECCV 2024*, Lecture Notes in Computer Science, vol. 15060. Cham, Switzerland: Springer, 2025, pp. 128–146, doi: 10.1007/978-3-031-72627-9_8.
- [22] S. D. Uhlich *et al.*, “OpenCap: Human movement dynamics from smartphone videos,” *PLOS Comput. Biol.*, vol. 19, no. 10, 2023, Art. no. e1011462, doi: 10.1371/journal.pcbi.1011462.

- [23] K. Werling *et al.*, “AddBiomechanics: Automating model scaling, inverse kinematics, and inverse dynamics from human motion data through sequential optimization,” *PLOS ONE*, vol. 18, no. 11, 2023, Art. no. e0295152, doi: 10.1371/journal.pone.0295152.
- [24] R. J. Cotton, “Differentiable biomechanics unlocks opportunities for markerless motion capture,” arXiv preprint arXiv:2402.17192, 2024.
- [25] E. Todorov, T. Erez, and Y. Tassa, “MuJoCo: A physics engine for model-based control,” in *Proc. IEEE/RSJ Int. Conf. Intell. Robots Syst.*, 2012, pp. 5026–5033, doi: 10.1109/IROS.2012.6386109.
- [26] W. R. Taylor *et al.*, “A comprehensive assessment of the musculoskeletal system: The CAMS-Knee data set,” *J. Biomech.*, vol. 65, pp. 32–39, 2017, doi: 10.1016/j.jbiomech.2017.09.022.
- [27] L. Riglet *et al.*, “3D motion analysis dataset of healthy young adult volunteers walking and running on overground and treadmill,” *Sci. Data*, vol. 11, no. 1, 2024, Art. no. 556, doi: 10.1038/s41597-024-03420-y.
- [28] S. Tripathi, L. Müller, C.-H. P. Huang, O. Taheri, M. J. Black, and D. Tzionas, “3D human pose estimation via intuitive physics,” in *Proc. IEEE/CVF Conf. Comput. Vis. Pattern Recognit.*, 2023, pp. 4713–4725, doi: 10.1109/cvpr52729.2023.00457.
- [29] A. Counsell, “University of Portsmouth - Dog Motion Capture,” YouTube video, Dec. 2, 2016. [Online]. Available: <https://www.youtube.com/watch?app=desktop&v=OYh0jBDjNf4>. Accessed: Mar. 18, 2024.
- [30] C. Li *et al.*, “The Poses for Equine Research Dataset (PFERD),” *Sci. Data*, vol. 11, no. 1, 2024, Art. no. 497, doi: 10.1038/s41597-024-03312-1.
- [31] J. L. Hicks, T. K. Uchida, A. Seth, A. Rajagopal, and S. L. Delp, “Is my model good enough? Best practices for verification and validation of musculoskeletal models and simulations of movement,” *J. Biomech. Eng.*, vol. 137, no. 2, 2015, Art. no. 020905, doi: 10.1115/1.4029304.
- [32] J. J. Dunne, T. K. Uchida, T. F. Besier, S. L. Delp, and A. Seth, “A marker registration method to improve joint angles computed by constrained inverse kinematics,” *PLOS ONE*, vol. 16, no. 5, 2021, Art. no. e0252425, doi: 10.1371/journal.pone.0252425.
- [33] M. A. Price, A. K. LaPrè, R. T. Johnson, B. R. Umberger, and F. C. Sup IV, “A model-based motion capture marker location refinement approach using inverse kinematics from dynamic trials,” *Int. J. Numer. Methods Biomed. Eng.*, vol. 36, no. 1, 2020, Art. no. e3283, doi: 10.1002/cnm.3283.
- [34] E. S. Grood and W. J. Suntay, “A joint coordinate system for the clinical description of three-dimensional motions: Application to the knee,” *J. Biomech. Eng.*, vol. 105, no. 2, pp. 136–144, 1983, doi: 10.1115/1.3138397.
- [35] S. L. Delp, F. C. Anderson, A. S. Arnold, P. Loan, A. Habib, C. T. John, E. Guendelman, and D. G. Thelen, “OpenSim: Open-source software to create and analyze dynamic simulations of movement,” *IEEE Trans. Biomed. Eng.*, vol. 54, no. 11, pp. 1940–1950, 2007, doi: 10.1109/TBME.2007.901024.
- [36] H. Kainz, H. X. Hoang, C. Stockton, R. S. Boyd, D. G. Lloyd, and C. P. Carty, “Accuracy and reliability of marker-based approaches to scale the pelvis, thigh, and shank segments in musculoskeletal models,” *J. Appl. Biomech.*, vol. 33, no. 5, pp. 354–360, 2017, doi: 10.1123/jab.2016-0282.
- [37] C. Reinschmidt *et al.*, “Tibiofemoral and tibioalcalneal motion during walking: External vs. skeletal markers,” *Gait Posture*, vol. 6, no. 2, pp. 98–109, 1997, doi: 10.1016/S0966-6362(97)01110-7.
- [38] R. Tranberg, T. Saari, R. Zügner, and J. Kärrholm, “Simultaneous measurements of knee motion using an optical tracking system and radiostereometric analysis (RSA),” *Acta Orthop.*, vol. 82, no. 2, pp. 171–176, 2011, doi: 10.3109/17453674.2011.570675.
- [39] A. Fändriks, R. Zügner, B. Shareghi, J. Kärrholm, and R. Tranberg, “Skin and cluster markers underestimate knee flexion during controlled motions. Evaluation of 12 patients with knee arthroplasty using radiostereometric analysis as reference,” *J. Biomech.*, vol. 182, 2025, Art. no. 112591, doi: 10.1016/j.jbiomech.2025.112591.
- [40] S. Wang *et al.*, “Validation of a portable marker-based motion analysis system,” *J. Orthop. Surg. Res.*, vol. 16, no. 1, 2021, Art. no. 425, doi: 10.1186/s13018-021-02576-2.
- [41] D. L. Benoit, D. K. Ramsey, M. Lamontagne, L. Xu, P. Wretenberg, and P. Renström, “Effect of skin movement artifact on knee kinematics during gait and cutting motions measured in vivo,” *Gait Posture*, vol. 24, no. 2, pp. 152–164, 2006, doi: 10.1016/j.gaitpost.2005.04.012.
- [42] D. L. Miranda, M. J. Rainbow, J. J. Crisco, and B. C. Fleming, “Kinematic differences between optical motion capture and biplanar videoradiography during a jump-cut maneuver,” *J. Biomech.*, vol. 46, no. 3, pp. 567–573, 2013, doi: 10.1016/j.jbiomech.2012.09.023.
- [43] C. V. Hammond *et al.*, “The neuromusculoskeletal modeling pipeline: MATLAB-based model personalization and treatment optimization functionality for OpenSim,” *J. NeuroEng. Rehabil.*, vol. 22, no. 1, 2025, Art. no. 112, doi: 10.1186/s12984-025-01629-5.

- [44] A. Leardini, L. Chiari, U. Della Croce, and A. Cappozzo, “Human movement analysis using stereophotogrammetry. Part 3: Soft tissue artifact assessment and compensation,” *Gait Posture*, vol. 21, no. 2, pp. 212–225, 2005, doi: 10.1016/j.gaitpost.2004.05.002.
- [45] A. Barré, J.-P. Thiran, B. M. Jolles, N. Theumann, and K. Aminian, “Soft tissue artifact assessment during treadmill walking in subjects with total knee arthroplasty,” *IEEE Trans. Biomed. Eng.*, vol. 60, no. 11, pp. 3131–3140, 2013, doi: 10.1109/TBME.2013.2268938.
- [46] M. S. Andersen, M. Damsgaard, J. Rasmussen, D. K. Ramsey, and D. L. Benoit, “A linear soft tissue artefact model for human movement analysis: Proof of concept using in vivo data,” *Gait Posture*, vol. 35, no. 4, pp. 606–611, 2012, doi: 10.1016/j.gaitpost.2011.11.032.
- [47] C. L. Dembia, N. A. Bianco, A. Falisse, J. L. Hicks, and S. L. Delp, “OpenSim Moco: Musculoskeletal optimal control,” *PLOS Comput. Biol.*, vol. 16, no. 12, 2020, Art. no. e1008493, doi: 10.1371/journal.pcbi.1008493.
- [48] J. T. Sturdy, A. K. Silverman, and N. T. Pickle, “Automated optimization of residual reduction algorithm parameters in OpenSim,” *J. Biomech.*, vol. 137, 2022, Art. no. 111087, doi: 10.1016/j.jbiomech.2022.111087.
- [49] B. J. Fregly, J. A. Reinbolt, and T. L. Chmielewski, “Evaluation of a patient-specific cost function to predict the influence of foot path on the knee adduction torque during gait,” *Comput. Methods Biomech. Biomed. Eng.*, vol. 11, no. 1, pp. 63–71, 2008, doi: 10.1080/10255840701552036.
- [50] F. Heinen, M. E. Lund, J. Rasmussen, and M. de Zee, “Muscle–tendon unit scaling methods of Hill-type musculoskeletal models: An overview,” *Proc. Inst. Mech. Eng. H, J. Eng. Med.*, vol. 230, no. 10, pp. 976–984, 2016, doi: 10.1177/0954411916659894.
- [51] L. Modenese, E. Ceseracciu, M. Reggiani, and D. G. Lloyd, “Estimation of musculotendon parameters for scaled and subject specific musculoskeletal models using an optimization technique,” *J. Biomech.*, vol. 49, no. 2, pp. 141–148, 2016, doi: 10.1016/j.jbiomech.2015.11.006.